

Electron-beam induced methane decomposition for in-situ carbon doping of hexagonal boron nitride

Barbara Maria Mayer^{1,2}, Manuel Längle^{1,3}, Umair Javed^{1,4},

Toma Susi¹, E. Harriet Åhlgren², and Jani Kotakoski¹

¹*University of Vienna, Faculty of Physics,
Boltzmannngasse 5, 1090 Vienna, Austria*

²*Uppsala University, Box 516, Uppsala, SE-751 20, Sweden*

³*Univ. Paris-Saclay, CNRS, Laboratoire de Physique des Solides, 91405, Orsay, France and*

⁴*University of Vienna, Vienna Doctoral School in Physics,
Boltzmannngasse 5, 1090 Vienna, Austria*

(Dated: May 28, 2026)

Abstract

Controlling the spatial incorporation of carbon into hexagonal boron nitride (hBN) is essential for engineering optically active defects, yet existing approaches lack nanoscale precision and control over the carbon supply. Here, we demonstrate a method for carbon doping of hBN using electron-beam irradiation in a low-pressure methane atmosphere, where the beam simultaneously generates vacancies and decomposes methane into individual carbon and hydrogen atoms. Using annular dark-field scanning transmission electron microscopy, we show that increasing the methane partial pressure suppresses pore growth and drives the formation of triangular boron-terminated pores through preferential hydrogen etching of nitrogen. Time-resolved electron energy-loss spectroscopy (EELS) mapping reveals progressive carbon incorporation into the lattice, accompanied by boron and nitrogen depletion. Carbon clustering occurs predominantly within the irradiated area: $84\pm 7\%$ of carbon-rich regions are confined to the area exposed to the electron beam, while some carbon atoms are also found to diffuse up to an average distance of 4.7 ± 0.5 nm beyond it. The incorporated carbon atoms arrange in a hexagonal pattern within the lattice, forming patches that do not exceed ~ 1 nm in size. Analysis of the EELS fine structure indicates modifications to the local electronic environment within these regions, with implications for the optical properties of the resulting carbon-related defects.

INTRODUCTION

Two-dimensional (2D) hexagonal boron nitride (hBN) is a one-atom-thick material composed of boron and nitrogen atoms in a honeycomb lattice. The alternating arrangement of two atomic species with different electronegativities leads to a large electronic band gap that can be exploited to create localized states by introducing point defects, such as vacancies or substitutional impurity atoms. These defects can act as single-photon emitters (SPEs) when the material is optically excited, and are particularly attractive because they can exhibit spectrally narrow emission lines [1, 2], ranging from ultraviolet to near-infrared, and demonstrate excellent photostability [3] even at room temperature [4]. As a result, point defects in hBN are promising for applications in quantum communication [5] and computing [6], as well as sensing [7].

While linking specific photon-emission signatures to particular defective atomic structures remains debated, in part because of challenges in their microscopic characterization [8], a

growing consensus suggests that, apart from the negatively charged boron vacancy [9], most single-photon emission in hBN originates from carbon-related defects [10–15]. Consequently, methods for deliberately introducing carbon atoms into the hBN lattice are of significant interest. One approach involves incorporating carbon during material synthesis [15–17], enabling large-scale production of carbon-doped hBN with a relatively uniform carbon distribution [18]. However, such bottom-up techniques offer limited control over the precise placement of individual carbon atoms. This limitation has motivated the development of post-synthesis doping methods that target specific regions after crystal formation. Techniques such as ion implantation [15, 19], post-growth carbon diffusion into vacancies [20], and focused-ion-beam patterning [21] can achieve site-specific doping, but they often induce lattice damage, require high processing temperatures, or involve complex fabrication steps. To address these issues, electron-beam-assisted carbon doping has emerged as an alternative for introducing carbon into hBN [22–24]. Notably, Park et al. [24] demonstrated the atomically precise insertion of carbon atoms from surface contamination into pre-existing point vacancies in hBN using a focused electron beam. While this work established atomic-scale control at individual defect sites, it relies on an uncontrolled carbon supply and on pre-existing defect sites, which limit control over the spatial extent and distribution of carbon-doped regions—an essential requirement for future applications of C-doped hBN.

To address these limitations, we introduce a method that simultaneously creates lattice vacancies and supplies carbon from a controlled source. Methane (CH_4) gas is introduced directly into the column of a scanning transmission electron microscopy (STEM) instrument, where the focused electron beam dissociates the molecules into atomic carbon and hydrogen. The same beam that drives dissociation also ejects boron and nitrogen atoms from the lattice [25], creating vacancies and small pores [26, 27] into which carbon can incorporate. This pathway allows us to control both the vacancy generation rate and the carbon supply without relying on pre-existing defect sites or an uncontrolled reservoir of contamination. We characterize this process using three complementary experimental approaches. First, we quantify how methane partial pressure alters pore growth rates and morphology using time-resolved medium-angle annular dark-field (MAADF) image stacks, revealing a transition from uncontrolled pore growth due to oxygen etching of boron [27] to saturation and boron-terminated triangular pore formation driven by preferential nitrogen etching by hydrogen. Second, time-resolved EELS maps tracking the spatial and temporal evolution of

boron, carbon, and nitrogen concentrations show that carbon progressively incorporates into the lattice as nanoscale patches, predominantly within the electron-beam-irradiated region. Third, high-resolution imaging after extended irradiation reveals the atomic arrangement of carbon in these patches, showing a hexagonal substitutional geometry with a characteristic size of ~ 1 nm. Taken together, our findings propose a route to spatially controlled, nanoscale carbon doping of hBN, with promising prospects for the deterministic engineering of carbon-related single-photon emitters.

RESULTS AND DISCUSSION

Samples were prepared by electrochemical delamination of chemical vapor deposition (CVD)-grown hBN from the copper substrate, followed by transfer onto QuantifoilTM Au TEM grids with 1.2 μm holes, as described in Ref. [28]. Before insertion into the microscope, the samples were baked in vacuum at ca. 150°C for approximately 12 h.

For the experiments, the Vienna Nion UltraSTEM 100 was operated at 60 kV. While this microscope has a base pressure of $\sim 1.5 \times 10^{-10}$ Torr in the objective area [29], at the time of these experiments, one of the bellows at the objective area had a minor leak, leading to a base pressure roughly an order of magnitude higher than this. Under these conditions, we expect the major molecular species in the residual vacuum to be water. Nevertheless, a leak valve mounted on a port near the objective area allows controlling the local atmosphere around the sample [27, 29, 30] without disrupting imaging up to pressures around 10^{-6} Torr. To introduce gas in a controlled manner, the pressure in the objective area is monitored by a gauge; however, the actual pressure at the sample is estimated to be ten times higher than the gauge reading [29]. All pressures stated here are from the objective-area gauge.

In the first set of experiments, we examined how methane affects pore growth. This study was motivated by recent findings that oxygen in the objective area accelerates pore growth and leads to the formation of the well-known triangular, nitrogen-terminated pores [26, 27]. In contrast, the role of hydrocarbons—such as methane, a common residual gas in vacuum chambers—has not yet been explored. Here, methane was introduced into the microscope objective area until partial pressures between $(8.0 \text{ to } 8.9) \times 10^{-8}$ Torr were reached. Once the pressure stabilized, time-resolved medium-angle annular dark-field (MAADF) image stacks were recorded over a 4×4 nm² field of view (FOV) with a dwell time of 16 μs and a

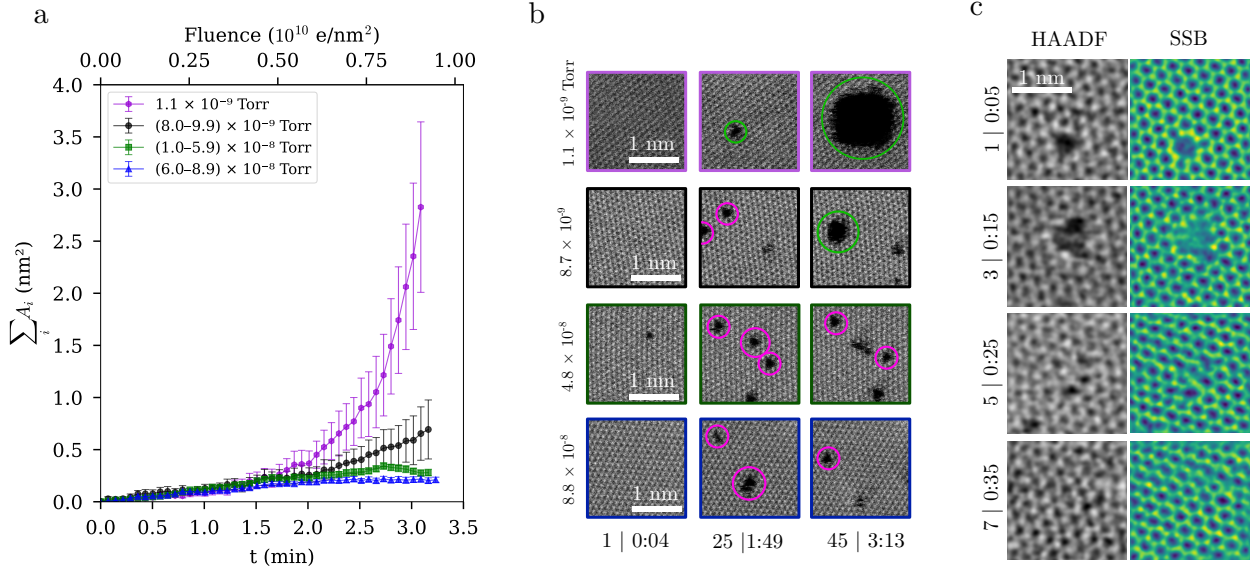


FIG. 1. Pore growth in an CH_4 atmosphere. (a) Total pore area within a $4 \times 4 \text{ nm}^2$ field of view as a function of time. Values are averaged over MAADF image stacks recorded at each pressure regime, with error bars indicating the standard error of the mean. The lowest pressure corresponds to no added methane in the column. (b) Selected frames from time-resolved MAADF image stacks recorded at 1.1×10^{-9} Torr (purple frames), 8.7×10^{-9} Torr (black frames), 4.8×10^{-8} Torr (green frames), and 8.8×10^{-8} Torr (blue frames), shown for the first recorded frame (0:04 min), the 25th frame (1:49 min), and the 45th frame (3:13 min). The green-circled defect corresponds to a pore with mixed boron and nitrogen termination, while the purple circles highlight pores with a triangular character and boron termination. (c) Selected frames from a time series showing concurrent filtered HAADF images (left column) and single-sideband (SSB) phase reconstructions (right column, false-colored with the viridis colormap) of pores at a methane partial pressure of 5.5×10^{-8} Torr, illustrating pore growth followed by filling.

size of 512×512 pixels. Each image was then analyzed semi-automatically using intensity thresholding to measure the total pore area over time.

As shown in Fig. 1(a), the pore-growth rate depends strongly on the methane partial pressure within the column. Before methane leakage, the pressure in the objective area was 1.1×10^{-9} Torr, and pore growth exhibited a quadratic trend. This behavior can be attributed to chemical etching by residual oxygen (either from water molecules or from molecular oxygen) in the column [27]. When methane is introduced at pressures of $(8.0$ to $9.9) \times 10^{-9}$ Torr, similar quadratic behavior remains, but the pore-growth rate decreases.

However, a substantial qualitative change in the growth rate occurs when the methane partial pressure is increased to $(1.0 \text{ to } 5.9) \times 10^{-8}$ Torr. Now, the pores tend to stabilize over time and eventually reach saturation, and, notably, in some cases, decrease in size, indicating partial pore filling. Further increases in methane partial pressure lead to even stronger suppression of pore growth. The pore-growth rate in this regime is comparable to the behavior reported for graphene under electron irradiation in ultra-high vacuum [31, 32].

In addition to affecting the pore-growth rate, variations in methane partial pressure within the column also cause distinct pore morphologies. At a pressure of 1.1×10^{-9} Torr, pores with boron- and nitrogen-terminated edges and a slight triangular character develop over time, as shown in the purple-enframed image sequence in Fig. 1(b). The slight triangular character can be explained by preferential etching of boron by residual oxygen [27]. When methane is introduced into the objective area, the pore morphology changes. At a pressure of 8.7×10^{-9} Torr, shown in the black-enframed image sequence in Fig. 1(b), triangular and metastable boron-terminated pores appear; however, they evolve into rounder pores with a mixed termination. Upon further increasing the methane partial pressure, relatively stable triangular boron-terminated pores form, as shown in the sequences framed in blue and green in Fig. 1(b), recorded at 4.8×10^{-8} and 8.8×10^{-8} Torr, respectively, though structural reconstruction and filling of pores is also observed, as shown in Fig. 1(c). In this image sequence, we observe a triangular pore corresponding to a tetravacancy forming first, growing somewhat over the next couple of images, and starting to fill, reaching a closed structure by frame 7 after only 35 s. The single-sideband ptychography images (shown in false color) allow the arrangement of atoms to be deduced in each frame, whereas the also shown HAADF images are less clear.

While it is natural to expect the filling of the pores to be related to carbon released by the dissociation of the methane molecules under the electron beam, it is much less clear what the cause is for the formation of triangular pores that terminate at the boron sublattice. Indeed, from either the ADF or SSB images, at the fast imaging parameters required to observe pore growth, it was difficult to reliably determine whether the atomic species at the edge is boron or carbon. Therefore, to better understand this, we carried out control experiments under a hydrogen atmosphere at 1.1×10^{-7} Torr. As shown in Fig. 2, under continuous electron irradiation, metastable triangular pores (mostly as a tetravacancy) with the same edge termination as those observed in a methane environment are present. The

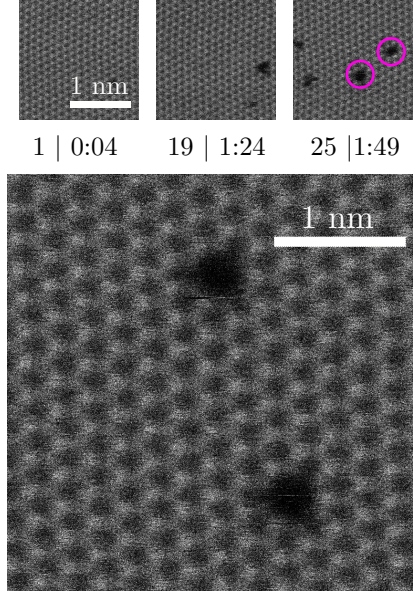


FIG. 2. MAADF images acquired at a hydrogen partial pressure of 1.1×10^{-7} Torr. The upper row shows the first (0:04 min), 19th (1:24 min), and 25th (1:49 min) recorded frames of an image series. The purple-encircled defects indicate triangular boron-terminated pores, two of which are clearly visible in the high-resolution MAADF image at the bottom.

increased stability of these structures under a hydrogen atmosphere also allows recording ADF images with much higher signal-to-noise, unambiguously showing that the edge atoms are boron. This suggests that hydrogen preferentially etches nitrogen and that the triangular pores observed under methane are terminated by boron rather than nitrogen.

Next, we return to pore filling. To gain insight into the elemental composition of the imaged sample area over time, we acquired sequential EELS maps. Each map was recorded over a 4×4 nm² area at methane partial pressures of $(1.0 \text{ to } 1.9) \times 10^{-7}$ Torr and across the 170–440 eV energy-loss range. This range was chosen to simultaneously observe the evolution of the B–*K* edge at 180 eV, the C–*K* edge at 284 eV, and the N–*K* edge at 402 eV. The energy scale was recalibrated using the separation of the B– and N–*K* edge π^* peaks, yielding a dispersion of 0.51 eV/channel. All EELS maps were acquired with a dwell time of 50 ms and at 64×64 pixels, resulting in a recording time of 3.4 min per map. The total duration of each experiment was between 25–35 min.

As shown in Fig. 3(a), carbon atoms that are progressively incorporated into the lattice over time tend to cluster together. In most cases, these patches appear to form via pore

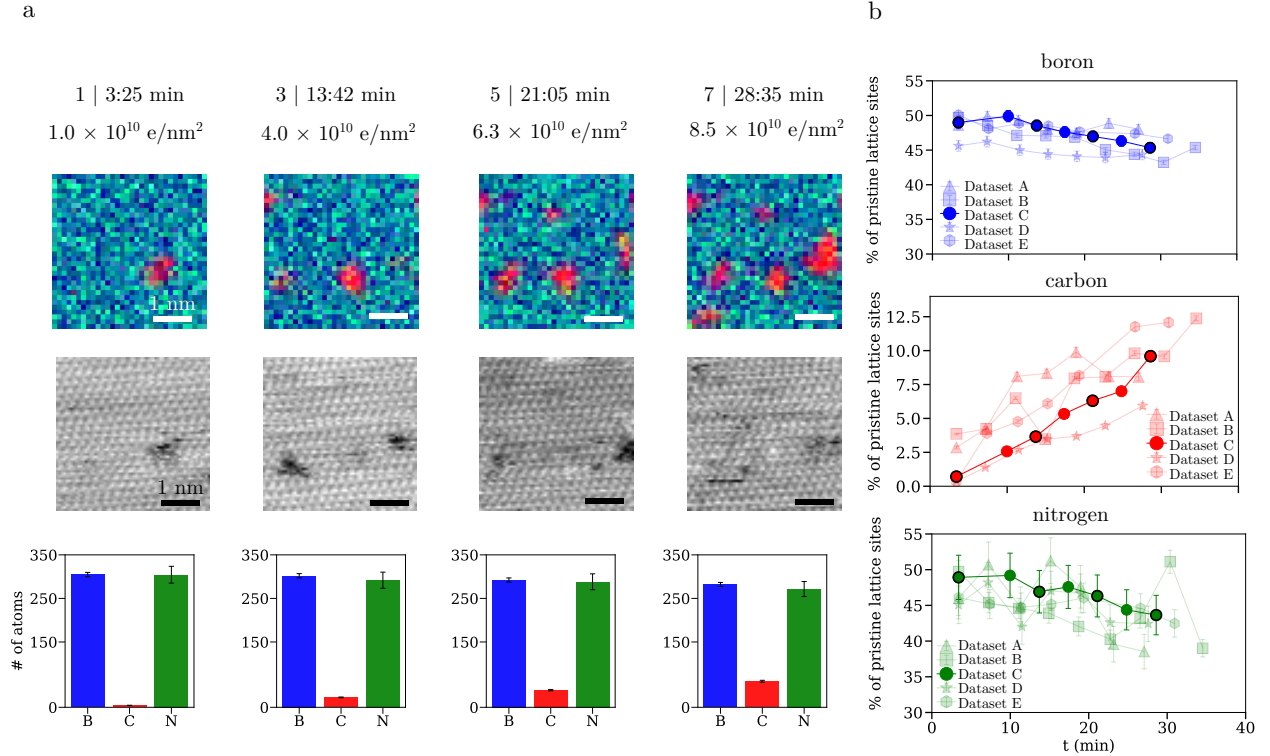


FIG. 3. Temporal evolution of carbon incorporation and concurrent boron and nitrogen depletion in hBN under electron-beam irradiation in a methane atmosphere at $(1.0 \text{ to } 1.9) \times 10^{-7}$ Torr. (a) The first row shows elemental maps derived from the integrated B-, C-, and N- K edge signals, shown in blue, red, and green, respectively. The second row presents the corresponding HAADF images recorded simultaneously. Scan artifacts are due to sample drift during the slow acquisition. The third row displays the numbers of B, C, and N atoms extracted from each frame, illustrating the progressive incorporation of carbon and the reduction of boron and nitrogen over time. (b) Relative areal fractions of boron, carbon, and nitrogen over time for five different datasets. A pristine hBN lattice corresponds to 50% boron and 50% nitrogen. The dataset shown in panel (a) is highlighted with opaque markers, while the remaining datasets are shown with semi-transparent symbols. Black-circled data points indicate the frames corresponding to those displayed in (a).

filling as shown above. However, particularly for smaller structures, a direct correspondence between a pore and carbon inclusion cannot always be established, likely because pore formation and healing occur on timescales shorter than the acquisition time of a single map. As shown in Fig. 3(b), across all five analyzed datasets, the amount of carbon in the first recorded EELS map is significantly lower than in the final frame. However, carbon

incorporation into the lattice is generally not constant over time, leading to variations in the absolute amount of carbon present.

As the carbon concentration in the lattice increases over time, the relative concentrations of boron and nitrogen decrease, as shown in Fig. 3(b). Similar to carbon incorporation, these changes are not uniform across all analyzed datasets. Nevertheless, a consistent trend emerges in which nitrogen is depleted from the lattice slightly more readily than boron. This observation aligns with previous experiments on the effect under a hydrogen atmosphere, which indicate preferential etching of nitrogen (in contrast to preferential etching of boron observed under an oxygen atmosphere [27]). However, it is worth noting that the absolute nitrogen concentration is associated with greater uncertainty because its K -edge is less intense than that of boron.

Having established that carbon incorporates into the lattice during the experiment, we turn to the question of spatial confinement. Overview EELS maps covering a 16×16 nm² field of view were acquired immediately before and after each central 4×4 nm² irradiation series, providing a direct measure of how far carbon spreads beyond the directly imaged area. In the pre-irradiation maps, carbon covers $0.4\pm 0.1\%$ of the imaged lattice area. After irradiation, the amount of carbon increases across all datasets; however, as noted above, the absolute rate of increase varies across datasets. Considering all C atoms in the post-irradiation maps individually, $29\pm 4\%$ fall within the irradiated region and $72\pm 4\%$ fall outside it, with those outside located, on average, 4.7 ± 0.5 nm from the irradiated boundary. This diffusion tail reflects the mobility of isolated carbon atoms under the electron beam and sets a practical limit on the precision of single-atom placement with the current approach. However, the picture changes when the analysis is restricted to carbon-dense regions—areas of 0.5×0.5 nm² containing three or more carbon atoms each. Of such regions, $84\pm 7\%$ are located within the irradiated area, and only $16\pm 7\%$ are outside. This distinction between single-atom diffusion and confinement of carbon-filled patches is important: the defects responsible for single-photon emission in hBN are thought to involve specific multi-atom carbon configurations [33], and our results suggest that such configurations form preferentially within the imaged area.

To atomically resolve the carbon patches and characterize their structure, we continuously imaged a 4×4 nm² FOV under 1.0×10^{-7} Torr methane partial pressure by recording 256×256 -pixel frames with a dwell time of 16 μ s and an electron dose rate of 4.9×10^7 e⁻/nm²s.

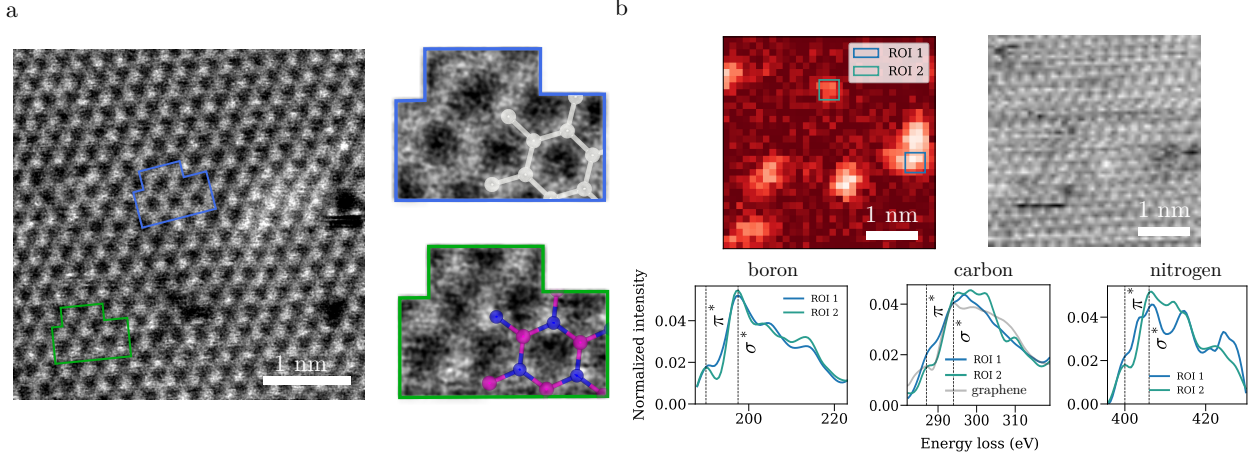


FIG. 4. Atomic structure and EELS fine structure of carbon patches formed in hBN. (a) High-resolution MAADF image of the hBN lattice after approximately 2.5 h of continuous electron irradiation at a methane pressure of 1.2×10^{-7} Torr. The blue frame highlights a region containing carbon atoms arranged in a hexagonal pattern; in the inset, white circles indicate carbon atoms. The green frame marks a pristine hBN region, where pink and blue circles respectively represent boron and nitrogen atoms. (b) Elemental map derived from the integrated C–*K* edge signal, together with representative EELS spectra extracted from selected regions of interest, marked on the elemental map. Spectra are normalized to their integrated area for comparison.

This dose rate was chosen to minimize pore formation during irradiation. In contrast to pore edges, where dynamic structural evolution under the electron beam prevents the acquisition of high signal-to-noise images, this limitation is absent within the basal plane. After approximately 2.5 h of continuous imaging, a high-resolution image of the exposed area was acquired with 1024×1024 pixels. This experiment was performed twice at different positions. As shown in Fig. 4(a), the atomically resolved images reveal patches of carbon atoms, consistent with the EELS-mapping results. Further, the images indicate that the carbon atoms preferentially adopt a hexagonal arrangement within the lattice, analogous to that in graphene.

To connect structural observations to changes in the electronic properties, we analyzed the EELS fine structure of carbon patches identified in the high-resolution imaging experiments. Regions of interest of 0.4×0.4 nm² were placed over carbon-containing areas of varying sizes, and the fine-structure fits within each region were averaged to reduce noise. The results reveal a clear dependence of the local electronic environment on patch size.

In smaller areas, the π^* peaks of the B- K , C- K , and N- K edges are well pronounced (Fig. 4(b), ROI 2), consistent with an sp^2 -bonded environment analogous to pristine hBN and graphene, respectively, where the π^* feature reflects delocalized bonding within the honeycomb lattice. In the central regions of larger patches with a nominal diameter of ~ 1 nm, however, the π^* intensities of both the B- K and C- K edges are suppressed relative to this reference (Fig. 4(b), ROI 1), indicating a disruption of the local bonding environment that cannot be attributed to pristine hBN or graphene-like carbon alone. This modification is consistent with the formation of a carbon-rich phase in which the surrounding boron and nitrogen sublattices are locally perturbed—a structural situation that is expected to generate localized electronic states within the hBN bandgap [34]. Whether such states give rise to optically active transitions at the single-photon level will require correlated optical measurements, but the observed fine-structure changes confirm that the incorporated carbon meaningfully alters the local electronic structure in a manner that is prerequisite for defect-based quantum emission.

CONCLUSION

We demonstrate a method for localized carbon doping of hexagonal boron nitride facilitated by electron-beam irradiation in a low-pressure methane atmosphere. We find that increasing the methane partial pressure suppresses pore growth and leads to the formation of boron-terminated triangular pores. Such structures, especially tetravacancies, are even more stable under a H_2 atmosphere, suggesting that they form due to preferential etching of nitrogen caused by hydrogen. In contrast, as revealed by time-resolved electron energy-loss spectroscopy maps, carbon dissociated from methane fills vacancies and pores created by boron and nitrogen depletion during electron irradiation. The incorporated carbon forms nanoscale patches that can be clearly attributed to electron-beam-induced doping, as shown by the strong spatial confinement of carbon-doped regions to the areas imaged with the electron beam. Additionally, we find that the carbon patches preferably adopt a hexagonal arrangement within the lattice and do not exceed ~ 1 nm in size. Changes in the EELS fine structure further indicate modifications to the local electronic environment within these clusters.

METHODS

Sample preparation

Samples were prepared using a chemical delamination method described in Ref. [28]. Commercial CVD-grown hBN on copper foil (Sigma-Aldrich) was cut into approximately $0.5 \times 0.5 \text{ cm}^2$ squares, slightly larger than the transmission electron microscopy (TEM) grids used as the final support. To stabilize the hBN during transfer, the surface was spin-coated with a thin layer of polymethyl methacrylate (PMMA, AR-P 642.04). Spin coating was performed in three stages: 500 rpm during dispensing, 1000 rpm for 15 s, and 2000 rpm for 60 s. The coated copper/hBN/PMMA stacks were then baked on a hot plate at 120°C for 10 min to harden the PMMA and improve adhesion to the hBN layer. After baking, the edges and one corner of the foil were trimmed with a surgical scalpel.

The hBN/PMMA layer was separated from the copper foil via electrochemical delamination. A platinum wire acted as the anode, while the copper foil, which was picked up at the scratched corner with inverse tweezers, served as the cathode in a NaOH solution (1 g NaOH in 25 g deionized water). Applying a 4.8 A bias caused hydrogen evolution on the copper surface, which detached the hBN/PMMA stack from the copper substrate. The detached film was gently rinsed in deionized water and scooped out using a Quantifoil TEM gold grid with $1.2 \text{ }\mu\text{m}$ radius holes and $1.3 \text{ }\mu\text{m}$ center-to-center spacing.

In the final step, the grids were placed on a glass slide and heated to 120°C for 12 min to dry the sample and ensure the adhesion of the hBN to the Quantifoil. The PMMA was then removed by immersing the grids in an acetone bath at 50°C for 1 h, followed by transferring them to isopropanol for 30 min to remove residual acetone and prevent damage from rapid evaporation. Upon insertion into the CANVAS [35], the samples were baked at ca. 150°C for ca. 12 h in vacuum.

Microscopy and spectroscopy

All experiments were performed using the aberration-corrected Vienna Nion UltraSTEM 100 operated at 60 kV, with a beam current estimated at 125 pA, as reported in Ref. [36]. The electron probe was formed with a convergence semi-angle of 34 mrad, yielding an effective probe size of $\sim 1.1 \text{ \AA}$. This customized STEM instrument enables gas introduction

into the column without compromising atomic-resolution imaging. Using this system, stable gas pressures of up to approximately 2×10^{-6} Torr can be achieved during imaging [29]. As noted in the main text, although this microscope has a base pressure of 1.5×10^{-10} Torr, it was about one order of magnitude higher during these experiments due to a minor leak. Under these conditions, we expect the major molecular species in the residual vacuum to be water when the leak valve is closed.

Imaging was performed using either a medium-angle (MAADF) or high-angle annular dark-field (HAADF) detector, with collection semi-angular ranges of 60–200 mrad and 80–300 mrad, respectively. The MAADF image series shown in Fig. 1 was recorded over a FOV of 4×4 nm² with a dwell time of 16 μ s and 512×512 pixels. Images were recorded at a partial pressure of 1.1×10^{-9} Torr (leak valve closed), methane partial pressures of 8.0×10^{-9} to 1.9×10^{-7} Torr, and a hydrogen partial pressure of 1.1×10^{-7} Torr, as measured by the objective-area pressure gauge.

Electron energy-loss spectroscopy (EELS) was conducted using a Gatan PEELS 666 spectrometer connected to an Andor iXon 897 electron-multiplying CCD camera. The spectrometer has 512 channels, a dispersion of 0.51 eV/channel, as revealed by the separation of the π^* peaks of the B- and N-*K* edges, and a collection semi-angle of 35 mrad [37]. All EELS maps were recorded with a 64×64 pixels and a dwell time of 50 ms, resulting in a recording time of 3.4 min per map. The FOVs were 4×4 nm² for EELS map series and 16×16 nm² for the overview maps, resulting in electron doses of 1.0×10^{-10} and 6.2×10^{-8} e⁻/nm² per map, respectively. The energy window for every map was set to 170–440 eV to simultaneously capture the evolution of the boron (~ 188 eV), carbon (~ 284 eV), and nitrogen (~ 402 eV) *K* edges. EELS maps were recorded at methane partial pressures of $(1.0$ to $1.9) \times 10^{-7}$ Torr.

Electron ptychography

For single-sideband (SSB) electron ptychography time-series acquisitions shown in Fig. 1(c), we recorded concurrent HAADF images and convergent-beam electron diffraction patterns for each of the 512×512 scan positions with a pixel dwell time of 10 μ s and a maximum scattering angle of 36 mrad on a Dectris ARINA detector binned by 16 [38]. All acquisitions were obtained under a methane partial pressure of 5.5×10^{-8} Torr. The SSB phase reconstructions used the quantitative electron microscopy (quantEM) data analysis toolkit [39]

(version 0.1.8 [40]). Residual electron-optical aberrations were corrected post-acquisition by least-squares fitting of their coefficients recursively up to 5th order using six \mathbf{q} -vectors in the double-disk overlap regions, with a signal weight of 0.25.

Data processing

ADF images

To quantify pore-growth rates, MAADF image stacks were analyzed using a semi-automated Python script, further described in Ref. [27]. For each frame, pores were identified by intensity thresholding, with low-intensity regions corresponding to vacancies, which were segmented and grouped into individual pores. The total pore area per image was obtained by summing the areas of all detected pores within the FOV. Scale calibration was performed using the lattice periodicity extracted from the fast Fourier transform (FFT) of the images, providing an accurate nanometer-per-pixel conversion. This calibration was then used to convert pore sizes from pixel units to physical areas.

For the filtered HAADF images in Fig. 1(c), after equalizing the image histograms to enhance contrast, we applied a double-Gaussian filter (with parameters $\sigma_1 = 9$ px, $\sigma_2 = 6$ px, $w = 0.3$), followed by a Butterworth high-pass filter to suppress low-frequency intensity variation presumably due to varying beam current (order 1, with a spatial frequency of $0.1/\text{px}$).

EELS maps

EELS maps were processed using the HyperSpy/eXSpy packages (versions 2.4.0 and 0.3.2, respectively) [41, 42]. Single-pixel intensity spikes attributed to cosmic-ray hits were removed before spatial binning by a factor of 2, reducing the map dimensions from 64×64 to 32×32 pixels. The spectra were then convolved with a 2 eV Gaussian to reduce noise in the fine-structure signals, and the energy axis calibrated by aligning the measured π^* peak positions of the B- and N-K edges with a reference spectrum from EELS.info [43], yielding a dispersion of 0.51 eV/channel (maximum allowed by our spectrometer). For each pixel, we first fitted the core-loss edges without a PowerLaw background using the ‘dft’ edge shape, with fitting windows of 187.5–223 eV, 282–319 eV, and 395.7–430.2 eV for the B-K,

C–*K*, and N–*K* edges, respectively. We then enabled the background and refitted; this two-step fitting procedure was found to improve numerical robustness. Fine structures for each edge were then iteratively fitted using the `multifit(kind='smart')` built-in functionality of HyperSpy/eXSpy, and the intensities of each edge were automatically corrected by the oscillator strengths for each core-level transition to obtain the elemental composition. Finally, negative edge intensities were constrained to positive values, and the model was refitted.

To convert fitted edge intensities into atom counts, the first map of each series served as a pristine hBN reference. The expected number of B and N atoms within the field of view was calculated geometrically from the hBN lattice constant ($a = 0.2504$ nm), yielding approximately 311 atoms per sublattice in the 4×4 nm² maps and approximately 4715 atoms per sublattice in the 16×16 nm² overview maps. The per-atom intensity for B and N was then determined by selecting a 10×10 -pixel ROI in a visually defect-free, carbon-free area of the first frame and dividing the total fitted edge intensity within that ROI by the corresponding expected atom count. The uncertainty was taken as the standard error of the mean (SEM) of the per-pixel intensities within the ROI. Since carbon is not present in each pixel, and because the C–*K* edge ionization cross-section lies between those of B and N, the carbon per-atom intensity was taken as the average of the B and N values, with the uncertainty propagated as the average of their respective SEMs.

ACKNOWLEDGEMENTS

ML acknowledges funding from the European Union’s Horizon Europe research and innovation programme under the Marie Skłodowska-Curie grant agreement No. 101210084. This research was funded in part by the Austrian Science Fund (FWF) [10.55776/COE5]. For open-access purposes, the author has applied a CC-BY public copyright license to any author-accepted manuscript version arising from this submission.

-
- [1] H. Akbari, S. Biswas, P. K. Jha, J. Wong, B. Vest, and H. A. Atwater, Lifetime-Limited and Tunable Quantum Light Emission in h-BN via Electric Field Modulation, *Nano Letters* **22**, 7798 (2022).

- [2] A. Dietrich, M. W. Doherty, I. Aharonovich, and A. Kubanek, Solid-state single photon source with Fourier transform limited lines at room temperature, *Physical Review B* **101**, 081401 (2020).
- [3] S. X. Li, T. Ichihara, H. Park, G. He, D. Kozawa, Y. Wen, V. B. Koman, Y. Zeng, M. Kuehne, Z. Yuan, S. Faucher, J. H. Warner, and M. S. Strano, Prolonged photostability in hexagonal boron nitride quantum emitters, *Communications Materials* 2023 4:1 **4**, 19 (2023).
- [4] G. Grosso, H. Moon, B. Lienhard, S. Ali, D. K. Efetov, M. M. Furchi, P. Jarillo-Herrero, M. J. Ford, I. Aharonovich, and D. Englund, Tunable and high-purity room temperature single-photon emission from atomic defects in hexagonal boron nitride, *Nature Communications* 2017 8:1 **8**, 1 (2017).
- [5] R. Hanson and D. D. Awschalom, Coherent manipulation of single spins in semiconductors, *Nature* 2008 453:7198 **453**, 1043 (2008).
- [6] J. L. O'Brien, Optical Quantum Computing, *Science* **318**, 1567 (2007).
- [7] R. Schirhagl, K. Chang, M. Loretz, and C. L. Degen, Nitrogen-vacancy centers in diamond: Nanoscale sensors for physics and biology, *Annual Review of Physical Chemistry* **65**, 83 (2014).
- [8] D. Lamprecht, S. Chokappa, A. M. Freilinger, B. M. Mayer, M. Melchior, J. Džibelová, D. Lorber, L. H. Tizei, M. Kociak, C. Mangler, L. Filipovic, and J. Kotakoski, Single photon emitters in hBN: Limitations of atomic resolution imaging and potential sources of error, *Ultramicroscopy* **282**, 114318 (2026).
- [9] V. Ivády, G. Barcza, G. Thiering, S. Li, H. Hamdi, J. P. Chou, O. Legeza, and A. Gali, Ab initio theory of the negatively charged boron vacancy qubit in hexagonal boron nitride, *npj Computational Materials* 2020 6:1 **6**, 41 (2020).
- [10] T. Vogl, V. Ivády, I. J. Luxmoore, and H. L. Stern, Defects in hexagonal boron nitride for quantum technologies: a perspective, *2D Materials* **13**, 023001 (2026).
- [11] R. Bourrellier, S. Meuret, A. Tararan, O. Stéphan, M. Kociak, L. H. Tizei, and A. Zobelli, Bright UV single photon emission at point defects in h-BN, *Nano Letters* **16**, 4317 (2016).
- [12] I. Zhigulin, K. Yamamura, V. Ivády, A. Gale, J. Horder, C. J. Lobo, M. Kianinia, M. Toth, and I. Aharonovich, Photophysics of blue quantum emitters in hexagonal boron nitride, *Materials for Quantum Technology* **3**, 015002 (2023).
- [13] T. T. Tran, C. Elbadawi, D. Totonjian, C. J. Lobo, G. Grosso, H. Moon, D. R. Englund, M. J. Ford, I. Aharonovich, and M. Toth, Robust multicolor single photon emission from point

- defects in hexagonal boron nitride, 2017 Conference on Lasers and Electro-Optics (CLEO) **2017-January**, 1 (2017).
- [14] S. A. Tawfik, S. Ali, M. Fronzi, M. Kianinia, T. T. Tran, C. Stampfl, I. Aharonovich, M. Toth, and M. J. Ford, First-principles investigation of quantum emission from hBN defects, *Nanoscale* **9** (2017).
- [15] N. Mendelson, D. Chugh, J. R. Reimers, T. S. Cheng, A. Gottscholl, H. Long, C. J. Mellor, A. Zettl, V. Dyakonov, P. H. Beton, S. V. Novikov, C. Jagadish, H. H. Tan, M. J. Ford, M. Toth, C. Bradac, and I. Aharonovich, Identifying carbon as the source of visible single-photon emission from hexagonal boron nitride, *Nature Materials* **20** (2021).
- [16] E. Williams, A. Gale, J. Horder, D. Scognamiglio, M. Toth, and I. Aharonovich, Quantum Emitters in Flux Grown hBN, *Crystal Growth and Design* **25**, 2083 (2025).
- [17] H. Liu, N. Mendelson, I. H. Abidi, S. Li, Z. Liu, Y. Cai, K. Zhang, J. You, M. Tamtaji, H. Wong, Y. Ding, G. Chen, I. Aharonovich, and Z. Luo, Rational Control on Quantum Emitter Formation in Carbon-Doped Monolayer Hexagonal Boron Nitride, *ACS Applied Materials and Interfaces* **14**, 3189 (2022).
- [18] T. W. Tang, R. Ritika, M. Tamtaji, H. Liu, Y. Hu, Z. Liu, P. R. Galligan, M. Xu, J. Shen, J. Wang, J. You, Y. Li, G. H. Chen, I. Aharonovich, and Z. Luo, Structured-Defect Engineering of Hexagonal Boron Nitride for Identified Visible Single-Photon Emitters, *ACS Nano* **19**, 8509 (2025).
- [19] D. Zhong, S. Gao, M. Saccone, J. R. Greer, M. Bernardi, S. Nadj-Perge, and A. Faraon, Carbon-Related Quantum Emitter in Hexagonal Boron Nitride with Homogeneous Energy and 3-Fold Polarization, *Nano Letters* **24**, 1106 (2024).
- [20] S. Ngamprapawat, J. Kawase, T. Nishimura, K. Watanabe, T. Taniguchi, K. Nagashio, S. Ngamprapawat, J. Kawase, T. Nishimura, K. Nagashio, K. Watanabe, and T. Taniguchi, From h-BN to Graphene: Characterizations of Hybrid Carbon-Doped h-BN for Applications in Electronic and Optoelectronic Devices, *Advanced Electronic Materials* **9**, 2300083 (2023).
- [21] Y. T. Wu, X. Guo, P. T. Jing, G. L. Liu, Z. Cheng, J. L. Xu, Y. Bao, H. Xu, L. G. Zhang, D. Zhan, J. X. Yan, L. Liu, and D. Z. Shen, Site-Controlled Carbon Implantation for Quantum Emitter Engineering in Hexagonal Boron Nitride, *ACS Applied Materials and Interfaces* **17**, 64864 (2025).

- [22] X. Wei, M. S. Wang, Y. Bando, and D. Golberg, Electron-beam-induced substitutional carbon doping of boron nitride nanosheets, nanoribbons, and nanotubes, *ACS Nano* **5** (2011).
- [23] X. Wei, M. S. Wang, Y. Bando, and D. Golberg, Post-synthesis carbon doping of individual multiwalled boron nitride nanotubes via electron-beam irradiation, *Journal of the American Chemical Society* **132** (2010).
- [24] H. Park, Y. Wen, S. Xin Li, W. Choi, G.-D. Lee, M. Strano, J. H. Warner, H. Park, J. H. Warner, Y. Wen, S. X. Li, M. Strano, W. Choi, and G.-d. Lee, Atomically Precise Control of Carbon Insertion into hBN Monolayer Point Vacancies using a Focused Electron Beam Guide, *Small* **17**, 2100693 (2021).
- [25] T. A. Bui, G. T. Leuthner, J. Madsen, M. R. Monazam, A. I. Chirita, A. Postl, C. Mangler, J. Kotakoski, and T. Susi, Creation of Single Vacancies in hBN with Electron Irradiation, *Small* **19** (2023).
- [26] J. Kotakoski, C. H. Jin, O. Lehtinen, K. Suenaga, and A. V. Krasheninnikov, Electron knock-on damage in hexagonal boron nitride monolayers, *Physical Review B - Condensed Matter and Materials Physics* **82** (2010).
- [27] U. Javed, C. Kofler, C. Mangler, and J. Kotakoski, Influence of low-pressure atmosphere in the pores formed in hexagonal boron nitride under electron irradiation, *arXiv* , 2507.13180 (2026).
- [28] P. Irschik, D. Lamprecht, S. Chokappa, C. Mangler, C. Speckmann, T. A. Bui, M. Längle, L. Filipovic, and J. Kotakoski, Atomically clean free-standing two-dimensional materials through heating in ultra-high vacuum, *2D Materials* **13**, 025001 (2026).
- [29] G. T. Leuthner, S. Hummel, C. Mangler, T. J. Pennycook, T. Susi, J. C. Meyer, and J. Kotakoski, Scanning transmission electron microscopy under controlled low-pressure atmospheres, *Ultramicroscopy* **203**, 76 (2019).
- [30] E. H. Åhlgren, A. Markevich, S. Scharinger, B. Fickl, G. Zagler, F. Herterich, N. McEvoy, C. Mangler, and J. Kotakoski, Atomic-Scale Oxygen-Mediated Etching of 2D MoS₂ and MoTe₂, *Advanced Materials Interfaces* **9** (2022).
- [31] G. T. Leuthner, T. Susi, C. Mangler, J. C. Meyer, and J. Kotakoski, Chemistry at graphene edges in the electron microscope, *2D Materials* **8**, 10.1088/2053-1583/abf624 (2021).
- [32] J. Kotakoski, D. Santos-Cottin, and A. V. Krasheninnikov, Stability of graphene edges under electron beam: Equilibrium energetics versus dynamic effects, *ACS Nano* **6**, 671 (2012).

- [33] S. Li, A. Pershin, G. Thiering, P. Udvarhelyi, and A. Gali, Ultraviolet Quantum Emitters in Hexagonal Boron Nitride from Carbon Clusters, *Journal of Physical Chemistry Letters* **13**, 3150 (2022).
- [34] Z. Qiu, K. Vaklinova, P. Huang, M. Grzeszczyk, K. Watanabe, T. Taniguchi, K. S. Novoselov, J. Lu, and M. Koperski, Atomic and Electronic Structure of Defects in hBN: Enhancing Single-Defect Functionalities, *ACS Nano* **18**, 24035 (2024).
- [35] C. Mangler, J. Meyer, A. Mittelberger, K. Mustonen, T. Susi, and J. Kotakoski, A Materials Scientist’s CANVAS: A System for Controlled Alteration of Nanomaterials in Vacuum Down to the Atomic Scale, *Microscopy and Microanalysis* **28**, 2940 (2022).
- [36] C. Speckmann, J. Lang, J. Madsen, M. R. A. Monazam, G. Zagler, G. T. Leuthner, N. McEvoy, C. Mangler, T. Susi, and J. Kotakoski, Combined electronic excitation and knock-on damage in monolayer MoS₂, *Physical Review B* **107**, 094112 (2023).
- [37] T. Susi, T. P. Hardcastle, H. Hofsäss, A. Mittelberger, T. J. Pennycook, C. Mangler, R. Drummond-Brydson, A. J. Scott, J. C. Meyer, and J. Kotakoski, Single-atom spectroscopy of phosphorus dopants implanted into graphene, *2D Materials* **4**, 021013 (2017).
- [38] T. Susi, Quantifying phase magnitudes of open-source focused-probe 4D-STEM ptychography reconstructions, *Journal of Microscopy* **300**, 201 (2025).
- [39] G. Varnavides, J. M. Bekkevold, S. M. Ribet, M. C. Scott, L. Jones, and C. Ophus, Relaxing direct ptychography sampling requirements via parallax imaging insights, *Microscopy and Microanalysis* (2025).
- [40] quantEM, Quantitative electron microscopy data analysis toolkit, <https://github.com/electronmicroscopy/quantem> (2026).
- [41] F. de la Peña, pburdet, M. Sarahan, magnunor, T. Ostasevicius, J. Taillon, A. Eljarrat, S. Mazzucco, vidartf, Gaël, L. F. Zagonel, M. Walls, and iygr, Hyperspy: HyperSpy 0.8, Zenodo (2015).
- [42] F. de la Peña, E. Prestat, P. Burdet, J. Lähnemann, K. E. MacArthur, V. T. Fauske, M. Sarahan, C. Francis, D. N. Johnstone, T. Ostasevicius, V. Migunov, T. Furnival, M. Nord, S. Mazzucco, A. Eljarrat, J. Caron, T. Aarholt, T. Poon, Z. Zhang, P. Jokubauskas, actions-user, F. Winkler, J. Taillon, T. Slater, pquinn-dls, G. Guzzinati, J. C. Myers, and N. Tappy, Hyperspy/exspy: V0.3.2, Zenodo (2025).
- [43] EELS.info, <https://eels.info/>, [Online; accessed 26-May-2026].

Supplemental Material

Electron-beam-induced carbon doping of hexagonal boron nitride

Dataset A

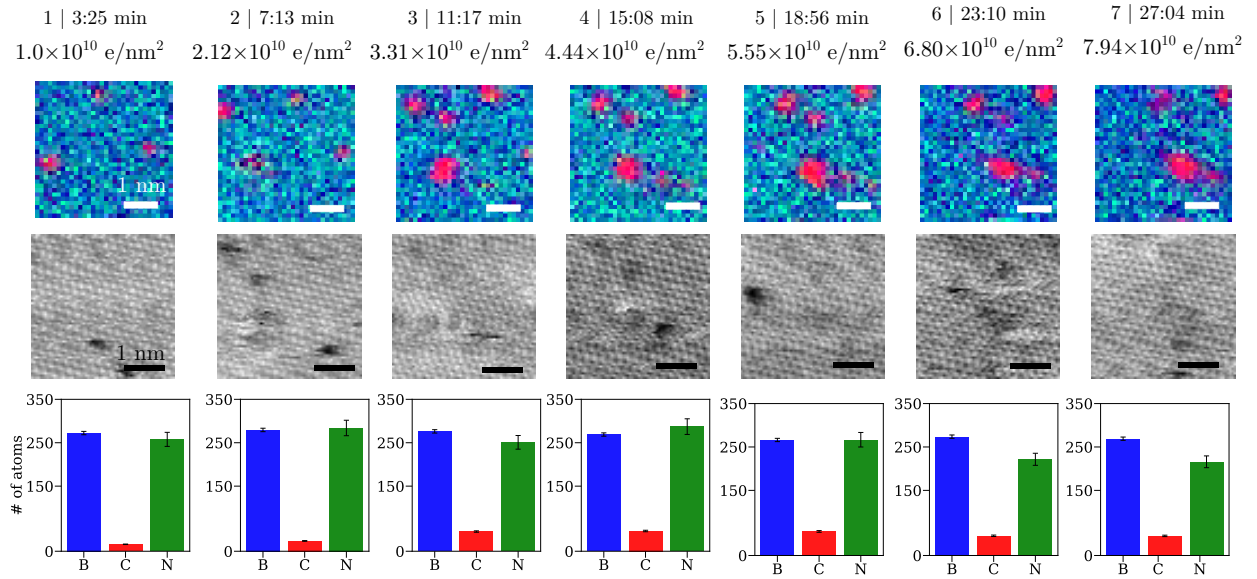


FIG. S1. Temporal evolution of carbon incorporation and concurrent boron and nitrogen depletion in hBN under electron-beam irradiation in a methane atmosphere at $(1.0 \text{ to } 1.9) \times 10^{-7}$ Torr for Dataset A. (a) The first row shows elemental maps derived from the integrated B-, C-, and N- K edge signals respectively represented in blue, red, and green. The second row presents the corresponding HAADF images acquired simultaneously with the elemental maps. The third row shows the quantified numbers of B, C, and N atoms extracted from each frame, illustrating the progressive incorporation of carbon together with the corresponding depletion of boron and nitrogen over time.

Dataset B

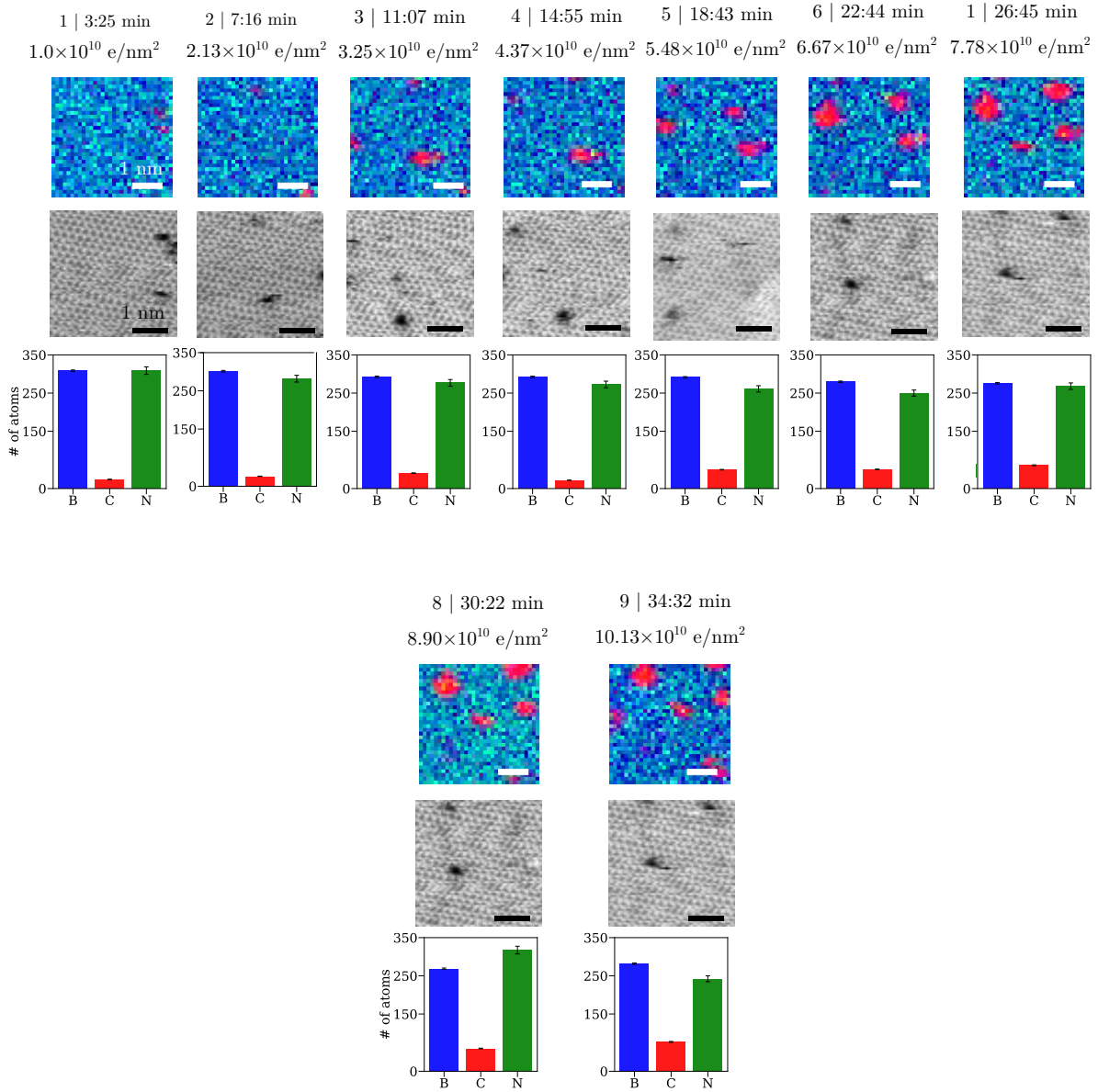


FIG. S2. Temporal evolution of carbon incorporation and concurrent boron and nitrogen depletion in hBN under electron-beam irradiation in a methane atmosphere at $(1.0 \text{ to } 1.9) \times 10^{-7}$ Torr for Dataset B. (a) The first row shows elemental maps derived from the integrated B-, C-, and N- K edge signals respectively represented in blue, red, and green. The second row presents the corresponding HAADF images acquired simultaneously with the elemental maps. The third row shows the quantified numbers of B, C, and N atoms extracted from each frame, illustrating the progressive incorporation of carbon together with the corresponding depletion of boron and nitrogen over time.

Dataset C

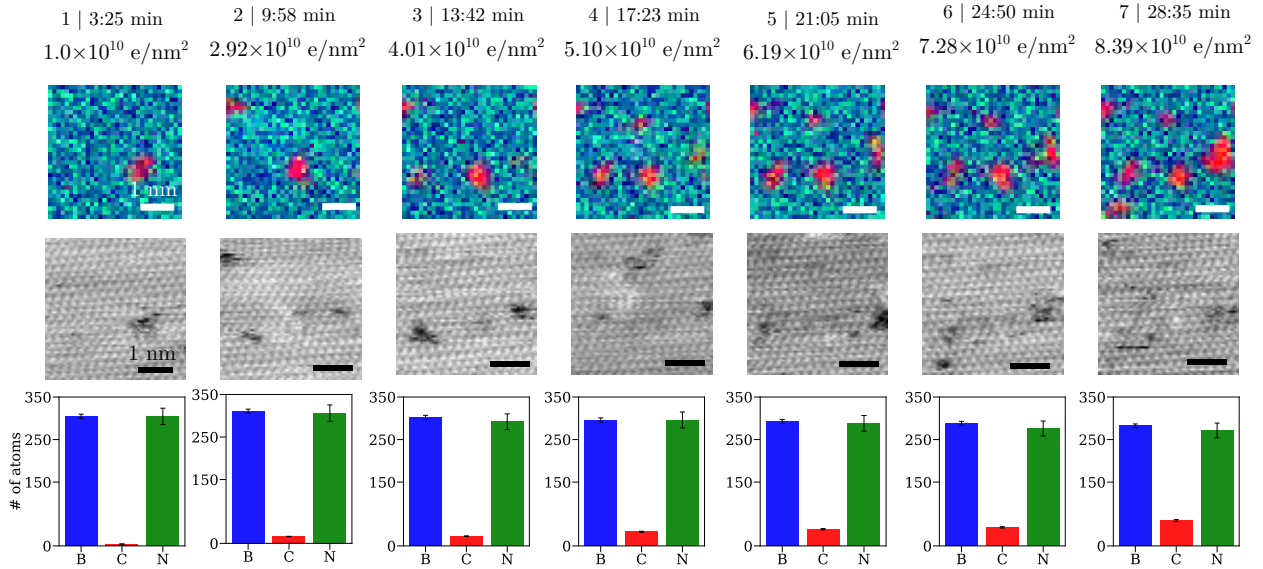


FIG. S3. Temporal evolution of carbon incorporation and concurrent boron and nitrogen depletion in hBN under electron-beam irradiation in a methane atmosphere at $(1.0 \text{ to } 1.9) \times 10^{-7}$ Torr for Dataset C. (a) The first row shows elemental maps derived from the integrated B-, C-, and N- K edge signals respectively represented in blue, red, and green. The second row presents the corresponding HAADF images acquired simultaneously with the elemental maps. The third row shows the quantified numbers of B, C, and N atoms extracted from each frame, illustrating the progressive incorporation of carbon together with the corresponding depletion of boron and nitrogen over time.

Dataset D

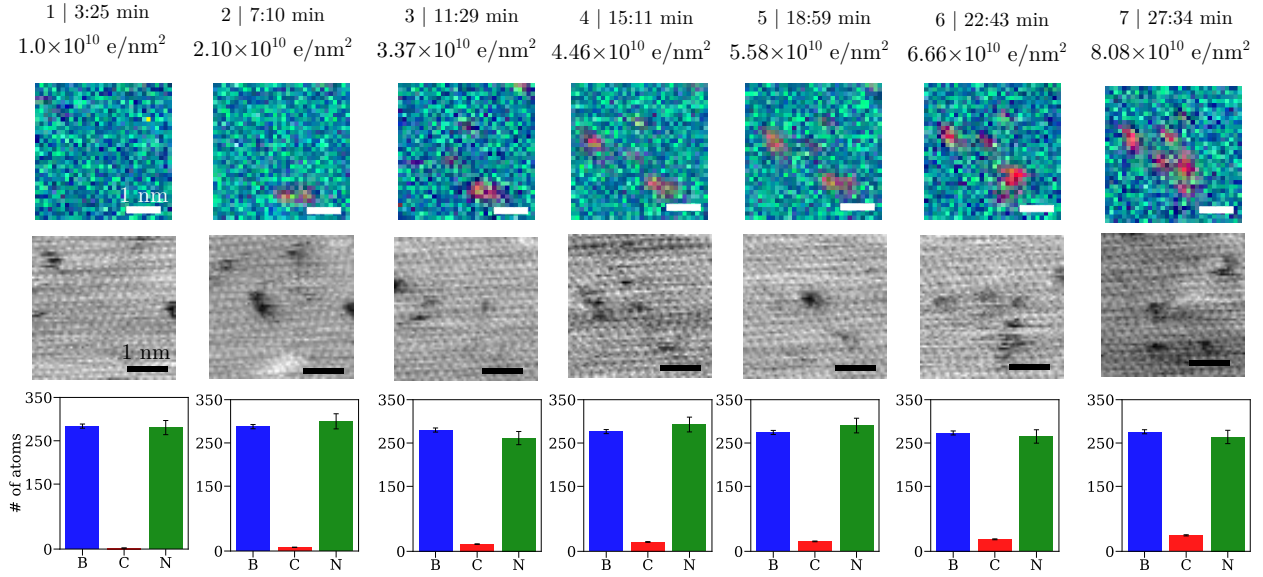


FIG. S4. Temporal evolution of carbon incorporation and concurrent boron and nitrogen depletion in hBN under electron-beam irradiation in a methane atmosphere at $(1.0 \text{ to } 1.9) \times 10^{-7}$ Torr for Dataset D. (a) The first row shows elemental maps derived from the integrated B-, C-, and N- K edge signals respectively represented in blue, red, and green. The second row presents the corresponding HAADF images acquired simultaneously with the elemental maps. The third row shows the quantified numbers of B, C, and N atoms extracted from each frame, illustrating the progressive incorporation of carbon together with the corresponding depletion of boron and nitrogen over time.

Dataset E

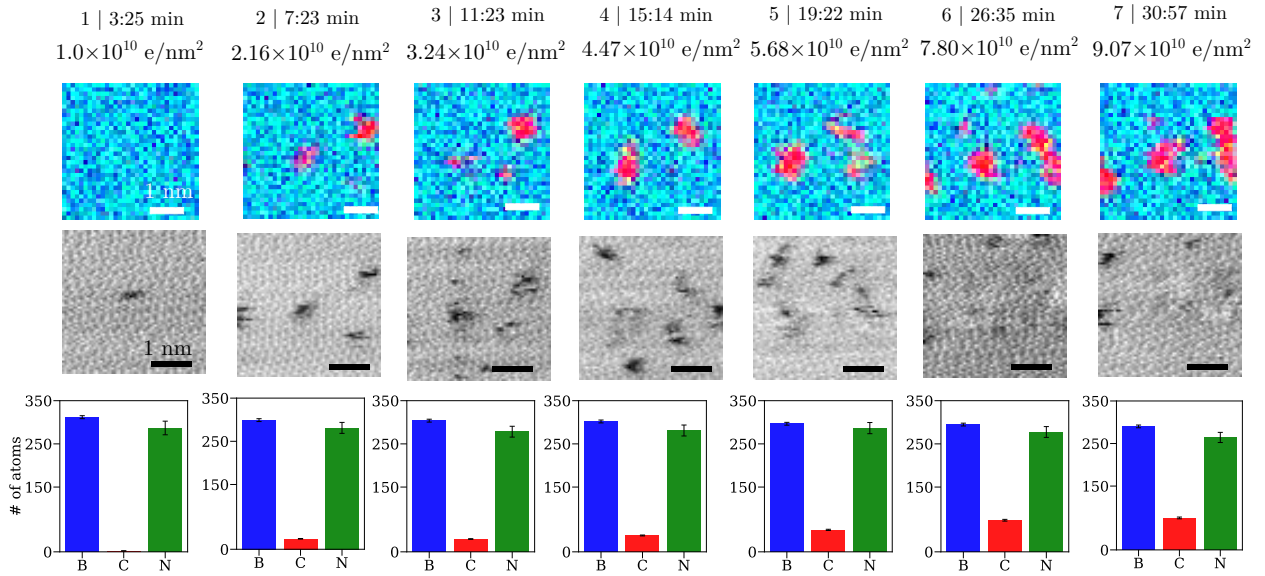


FIG. S5. Temporal evolution of carbon incorporation and concurrent boron and nitrogen depletion in hBN under electron-beam irradiation in a methane atmosphere at $(1.0 \text{ to } 1.9) \times 10^{-7}$ Torr for Dataset E. (a) The first row shows elemental maps derived from the integrated B-, C-, and N- K edge signals respectively represented in blue, red, and green. The second row presents the corresponding HAADF images acquired simultaneously with the elemental maps. The third row shows the quantified numbers of B, C, and N atoms extracted from each frame, illustrating the progressive incorporation of carbon together with the corresponding depletion of boron and nitrogen over time.

Dataset A

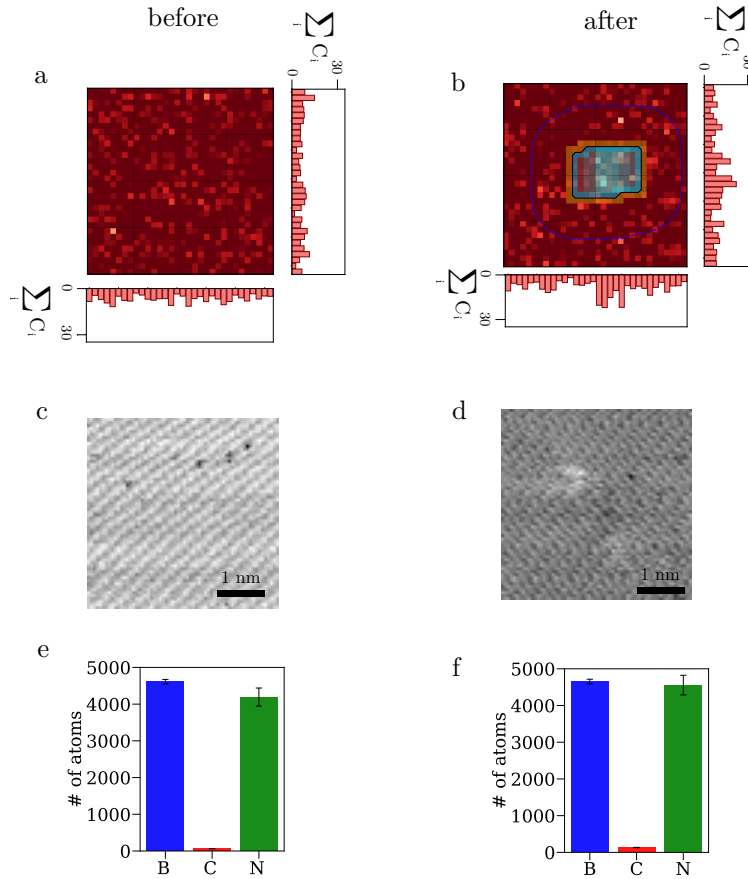


FIG. S6. Overview EELS maps for Dataset A. (a) Heatmap showing the carbon abundance across a $16 \times 16 \text{ nm}^2$ field of view (FOV), acquired before the $4 \times 4 \text{ nm}^2$ FOV EELS map series shown in Fig. S1. The blue-highlighted region enclosed by the black outline indicates the area exposed to the electron beam, while the orange region represents the uncertainty in the electron-beam position. The blue dashed line indicates the average distance between carbon atoms located outside the electron-beam-irradiated region and the irradiated region itself. The histograms below and to the right of the heatmap show the respective summed carbon-atom counts for the columns and rows of the map. (b) Heatmap showing the carbon abundance across a $16 \times 16 \text{ nm}^2$ FOV, acquired after the $4 \times 4 \text{ nm}^2$ FOV EELS map series shown in Fig. S1. (c)–(d) Concurrent HAADF images corresponding to the overview maps shown in (a) and (b). (e)–(f) Amounts of boron, carbon, and nitrogen detected in the EELS maps acquired before and after the central map series.

Dataset B

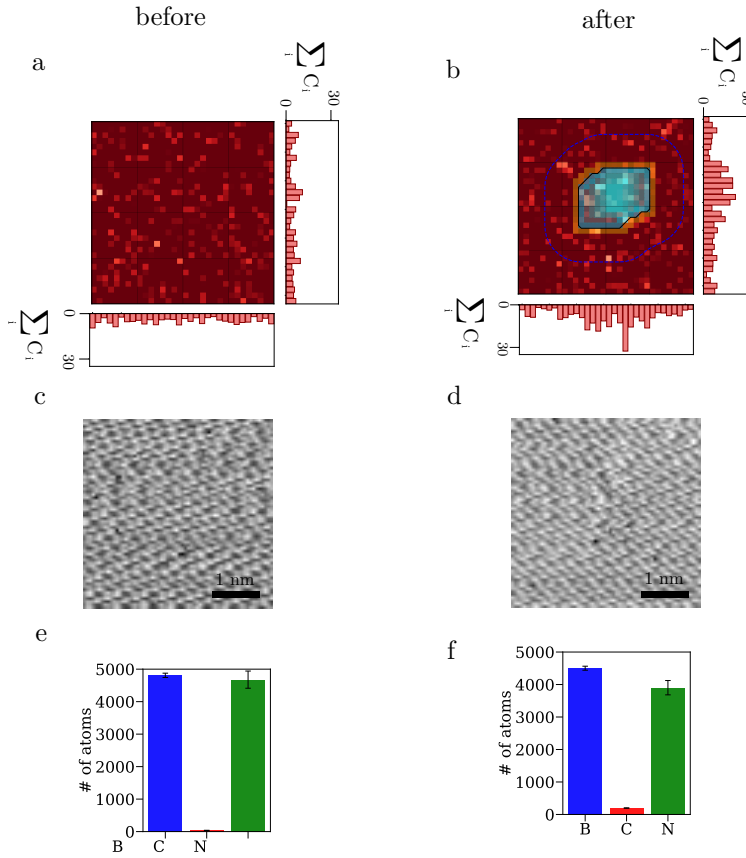


FIG. S7. Overview EELS maps for Dataset B. (a) Heatmap showing the carbon abundance across a $16 \times 16 \text{ nm}^2$ field of view (FOV), acquired before the $4 \times 4 \text{ nm}^2$ FOV EELS map series shown in Fig. S2. The blue-highlighted region enclosed by the black outline indicates the area exposed to the electron beam, while the orange region represents the uncertainty in the electron-beam position. The blue dashed line indicates the average distance between carbon atoms located outside the electron-beam-irradiated region and the irradiated region itself. The histograms below and to the right of the heatmap show the respective summed carbon atom counts for the columns and rows of the map. (b) Heatmap showing the carbon abundance across a $16 \times 16 \text{ nm}^2$ FOV, acquired after the $4 \times 4 \text{ nm}^2$ FOV EELS map series shown in Fig. S2. (c)–(d) Concurrent HAADF images corresponding to the overview maps shown in (a) and (b). (e)–(f) Amounts of boron, carbon, and nitrogen detected in the EELS maps acquired before and after the central map series.

Dataset C

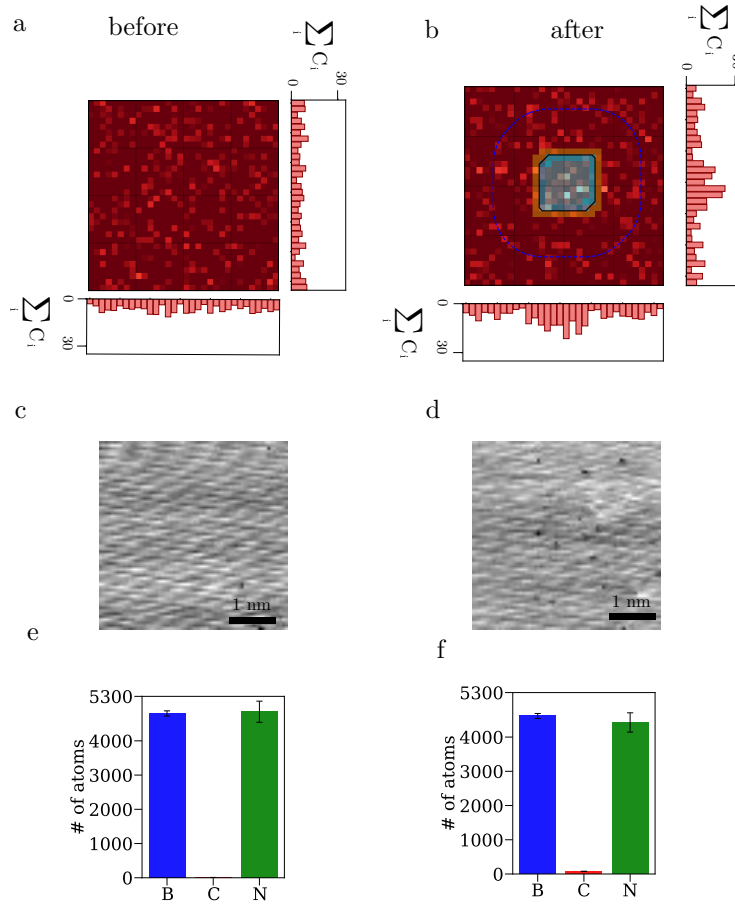


FIG. S8. Overview EELS maps for Dataset C. (a) Heatmap showing the carbon abundance across a $16 \times 16 \text{ nm}^2$ field of view (FOV), acquired before the $4 \times 4 \text{ nm}^2$ FOV EELS map series shown in Fig. S3. The blue-highlighted region enclosed by the black outline indicates the area exposed to the electron beam, while the orange region represents the uncertainty in the electron-beam position. The blue dashed line indicates the average distance between carbon atoms located outside the electron-beam-irradiated region and the irradiated region itself. The histograms below and to the right of the heatmap show the respective summed carbon atom counts for the columns and rows of the map. (b) Heatmap showing the carbon abundance across a $16 \times 16 \text{ nm}^2$ FOV, acquired after the $4 \times 4 \text{ nm}^2$ FOV EELS map series shown in Fig. S3. (c)–(d) Concurrent HAADF images corresponding to the overview maps shown in (a) and (b). (e)–(f) Amounts of boron, carbon, and nitrogen detected in the EELS maps acquired before and after the central map series.

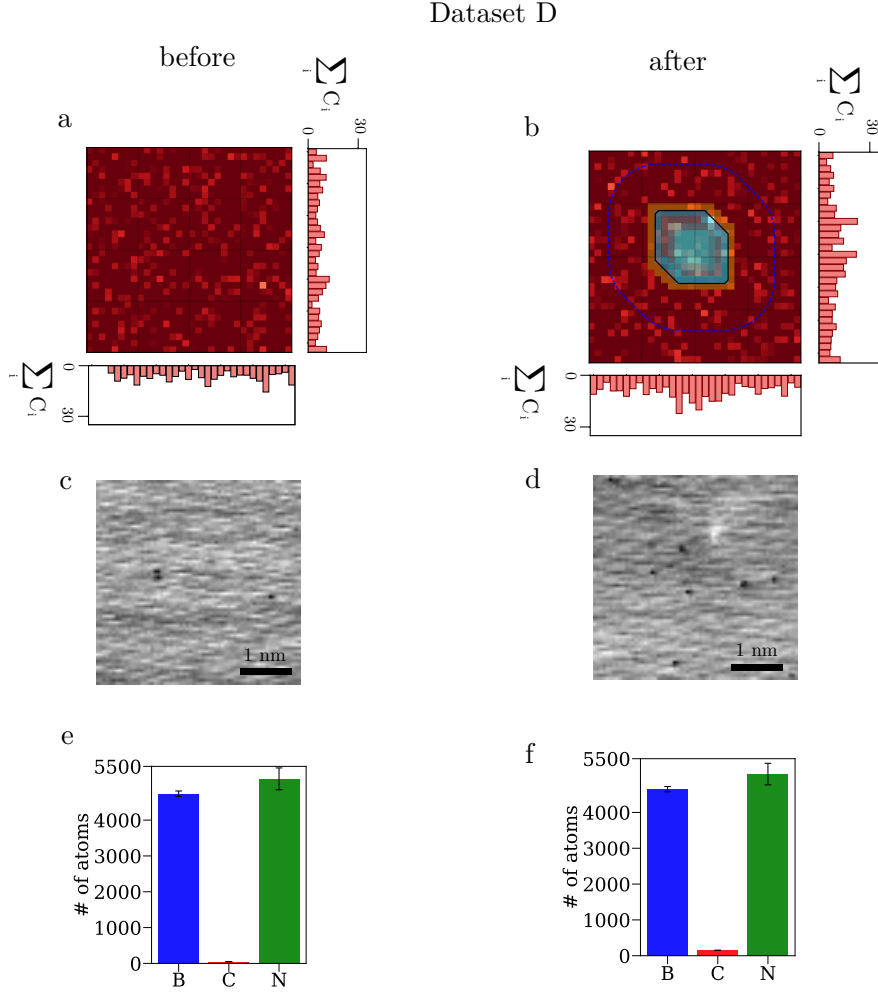


FIG. S9. Overview EELS maps for Dataset D. (a) Heatmap showing the carbon abundance across a $16 \times 16 \text{ nm}^2$ field of view (FOV), acquired before the $4 \times 4 \text{ nm}^2$ FOV EELS map series shown in Fig. S4. The blue-highlighted region enclosed by the black outline indicates the area exposed to the electron beam, while the orange region represents the uncertainty in the electron-beam position. The blue dashed line indicates the average distance between carbon atoms located outside the electron-beam-irradiated region and the irradiated region itself. The histograms below and to the right of the heatmap show the respective summed carbon atom counts for the columns and rows of the map. (b) Heatmap showing the carbon abundance across a $16 \times 16 \text{ nm}^2$ FOV, acquired after the $4 \times 4 \text{ nm}^2$ FOV EELS map series shown in Fig. S4. (c)–(d) Concurrent HAADF images corresponding to the overview maps shown in (a) and (b). (e)–(f) Amounts of boron, carbon, and nitrogen detected in the EELS maps acquired before and after the central map series.